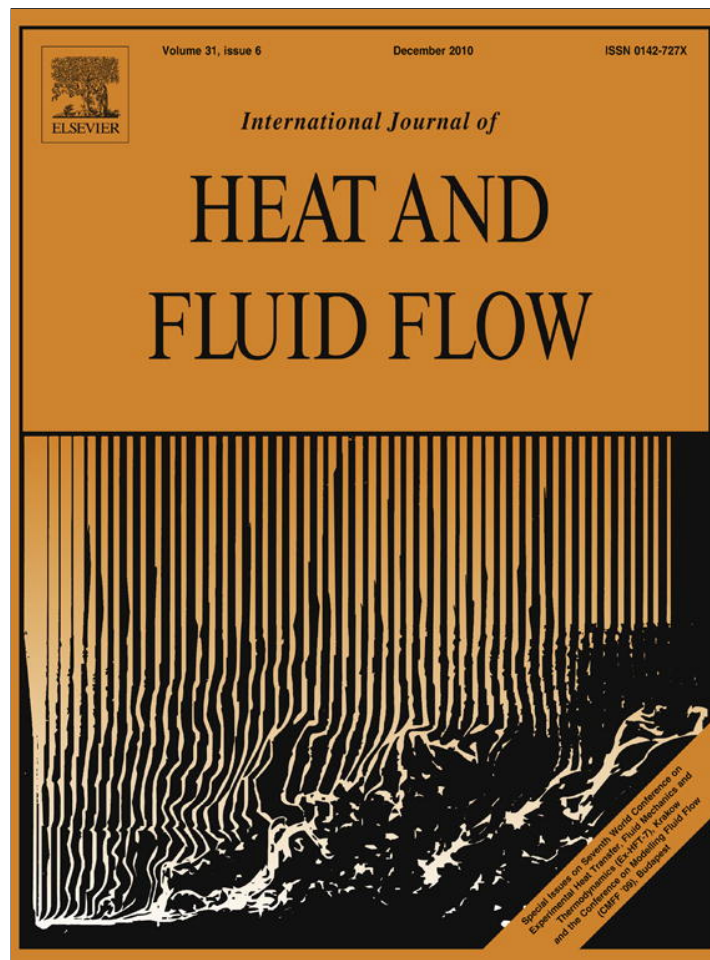


Provided for non-commercial research and education use.
Not for reproduction, distribution or commercial use.



This article appeared in a journal published by Elsevier. The attached copy is furnished to the author for internal non-commercial research and education use, including for instruction at the authors institution and sharing with colleagues.

Other uses, including reproduction and distribution, or selling or licensing copies, or posting to personal, institutional or third party websites are prohibited.

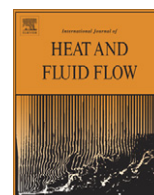
In most cases authors are permitted to post their version of the article (e.g. in Word or Tex form) to their personal website or institutional repository. Authors requiring further information regarding Elsevier's archiving and manuscript policies are encouraged to visit:

<http://www.elsevier.com/copyright>



Contents lists available at ScienceDirect

International Journal of Heat and Fluid Flow

journal homepage: www.elsevier.com/locate/ijhff

RANS-based numerical simulation and visualization of the horseshoe vortex system in the leading edge endwall region of a symmetric body

A.M. Levchenya^a, E.M. Smirnov^a, V.D. Goryachev^{b,*}

^a Department of Aerodynamics, St.-Petersburg State Polytechnic University, 195251 St. Petersburg, Russia

^b Department of Mathematics, Tver State Technical University, 170026 Tver, Russia

ARTICLE INFO

Article history:

Received 15 December 2009

Received in revised form 7 May 2010

Accepted 30 June 2010

Available online 27 July 2010

Keywords:

Horseshoe vortex
Wing-body juncture
Endwall heat transfer
RANS
Flow visualization

ABSTRACT

This contribution is aimed at analyzing the capabilities of popular two-equation turbulence models to predict features of 3D flow fields and endwall heat transfer near the blunt edge of a symmetric body mounted on a plate. The configuration studied experimentally by Praisner and Smith is considered. Results obtained with the in-house CFD code SINF and the commercial package ANSYS–CFX are presented and compared. Prediction capabilities of the low-*Re* Wilcox turbulence model and two versions of the Menter SST model, the original and the modified one, are analyzed in comparison with the experimental data. Special attention is paid to grid sensitivity of the numerical solutions. Advanced visualization of the vortex structures computed is performed with author's visualization tool HDVIS. It has been established that the Wilcox model is not capable of predicting the development of a multiple-vortex system observed in the experiment upstream of the body leading edge. Both versions of the MSST model produce qualitatively correct results, with a considerable superiority of the modified version when compared with the quantitative data.

© 2010 Elsevier Inc. All rights reserved.

1. Introduction

For flow configurations with a boundary layer approaching an obstruction in the form of a bluff body or a blunt-nose wing, it is well known that the body-generated adverse pressure gradient creates a three-dimensional separation, which forces the boundary layer vorticity to reorganize into a horseshoe vortex system (Simpson, 2001). Typically this system consists of a primary horseshoe vortex (HV), a counter-rotating secondary vortex (SV), and a tertiary vortex (TV). Moreover, as established in (Devenport and Simpson, 1990) via hot-wire measurements of the turbulent flow field near a symmetrical airfoil mounted on a flat plate, the horseshoe vortex system upstream of the airfoil leading edge is subjected to bimodal, low-frequency oscillations. This dynamic behavior of the vortex system can be a source of discrepancies between instantaneous and time-mean flow topologies. This aspect has been investigated extensively in the recent experimental study by Praisner and Smith (2006a,b) where the turbulent flow around a symmetric streamlined cylinder and associated endwall heat transfer were measured simultaneously with the PIV method and the thermochromic liquid–crystal technique.

If there is a temperature difference between the free-stream and endwall, horseshoe vortex structures generate specific varia-

tions of local heat transfer. In the case of multiple vortices, alternate in- and outflows developing in the vicinity of the endwall change the thermal boundary layer thickness that results in a non-monotonic variation of heat transfer intensity (Praisner and Smith, 2006a,b).

Flows in various generic junction configurations have been extensively studied numerically using steady-state Reynolds-averaged Navier–Stokes (RANS) turbulence models, including linear and nonlinear eddy-viscosity models and second-moment closure models (Bonnin et al., 1996; Batten et al., 1999; Apsley and Leschziner, 2001). In particular, data of experimental study of wing-body junction (Devenport and Simpson, 1990) were used in extended test computations (Apsley and Leschziner, 2001) aimed at analyzing capabilities of more than 10 turbulence models, among which the best results were shown by the Menter SST eddy-viscosity model (Menter, 1993) and second-moment models. However, knowledge of RANS models capabilities for reproducing local heat transfer in junction configurations is quite limited. Moreover, numerical solutions with multiple horseshoe vortices may be rather sensitive to grid resolution as well as to concrete CFD code realization of a turbulence model.

The present numerical study was performed under conditions that corresponded to the configuration used in the experimental work of (Praisner and Smith, 2006a,b). The computations were performed using two 3D CFD codes, namely the commercial package ANSYS–CFX (ANSYS Inc., 2006) and the in-house code SINF being under long-time development at the Department of Aerodynamics

* Corresponding author. Tel.: +7 4822444788.

E-mail addresses: aero@phmf.spbstu.ru (A.M. Levchenya), valery@tversu.ru (V.D. Goryachev).

Nomenclature

C	specific heat (J/kg K)	φ	azimuthal angle ($^{\circ}$)
d	cylinder diameter (m)	λ_0	distance between the primary HV axis and the body leading edge (LE) in the symmetry-plane (m)
Pr	Prandtl number (-)	λ_s	distance between the separation point (SP) and the body LE in the symmetry plane (m)
q	wall heat flux (W/m ²)	ρ	density (kg/m ³)
Q	Q -criterion (1/s ²)	Ω	vorticity magnitude (1/s)
Re	Reynolds number (-)		
St	Stanton number (-)		
T	temperature (K)		
V	velocity (m/s)		
Y^+	normalized distance to the wall for the first computational point (-)		
X, Y, Z	Cartesian coordinates (m)		
δ^*	boundary layer (BL) displacement thickness (m)		
δ	BL thickness (99% level) (m)		
Δ^*	specific cell size in the region of primary horseshoe vortex (HV) formation (m)		
		<i>Subscripts and Superscripts</i>	
		<i>in</i>	inlet free-stream value
		<i>t</i>	turbulent
		<i>w</i>	wall
		<i>max</i>	maximum

of the St.-Petersburg State Polytechnic University (Smirnov and Zaitsev, 2004a,b). Several low- Re turbulence models of the k - ω family were examined in comparison with the experimental data. For visualization of the vortex structures computed, the new recently developed software HDVIS (Zaitsev et al., 2008) was employed.

2. Problem definition

2.1. Basic statements

Fig. 1 illustrates the experimental configuration studied in the work of Praisner and Smith (2006a,b). A 15.08 cm diameter cylinder with a 5:1 trailing edge fairing was used as a blunt-nose body mounted on a flat test plate, with localized heating applied in the endwall region. The experiments were carried out in the open water channel 0.9 m width, the water depth was of about 0.4 m.

The free-stream water velocity, V_{in} , was equal to 0.147 m/s that gave the Reynolds number, based on this velocity and the cylinder diameter, equal to 2.44×10^4 . The free-stream water temperature, T_{in} , was kept at 25 °C. A constant heat flux, q , of 10,500 W/m² was provided over the 0.3×0.3 m endwall segment in the vicinity of the body leading edge, as shown in Fig. 1. Remaining walls were thermally insulated.

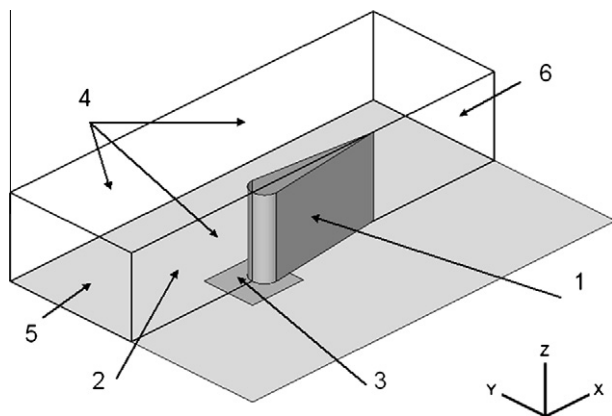


Fig. 1. Scheme of the flow domain: a blunt-nose body (1) mounted on the plate (2), and a part of which (3) is heated. Computational domain boundaries are shown as well: symmetry (4), inlet (5) and outlet (6) planes.

The governing equations used for the present steady-state computations are the Reynolds-averaged incompressible-fluid Navier-Stokes equations and the energy equation.

As a result of preliminary computations, it has been established that the maximum temperature difference between the free-stream and the heater surface is about 15 °C, and variations of the water viscosity do not exceed 25%. Such a level of viscosity variations does not affect noticeably any of the flow characteristics considered below. Consequently, the program of the present computations was based on the assumption of the constant physical properties of the fluid. The Prandtl number, Pr , was set to 6.3 that corresponds to the value at the free-stream temperature.

For turbulence modelling, low- Re turbulence models of the k - ω family were employed. The Wilcox model (Wilcox, 1993), added by the Kato-Lauder correction (Kato and Launder, 1993), and the original version of the Menter SST (MSST) (Menter, 1993) were used in the first stages of the present study. The second stage computations were performed using the MSST model, mostly in its modified form that is given in (Menter et al., 2003) and implemented in the last releases of the ANSYS-CFX. In all the computations the turbulent Prandtl number, Pr_t , was taken as 0.9.

2.2. Boundary conditions

The computational domain shown in Fig. 1 has a form of a parallelepiped whose faces are parallel to the Cartesian system axes. The inlet section is placed 1.5 m upstream of the cylinder, and the outlet section is positioned 1.5 m downstream of the body trailing edge.

The lateral size of domain was defined as the experimental channel halfwidth reduced by a characteristic displacement thickness, δ^* , of the side-wall boundary layer at the body leading edge position. A value of $\delta^* = 6 \times 10^{-3}$ m was taken as a result of preliminary computations of two-dimensional (2D) turbulent boundary layer development.

The 3D computations were performed with the symmetry condition in the middle longitudinal plane, perpendicular to the endwall, $Y = 0$. The symmetry condition was used also at the outer boundary, $Y = Y_{max}$. At the solid surfaces of the body-plate juncture the no-slip condition was imposed. For the computational domain plane parallel to the plate, $Z_{max} = 0.4$ m, the slip condition (equivalent in this case to the symmetry condition) was prescribed taking into account that the experiments (Praisner and Smith, 2006a,b) were carried out in the open water channel and neglecting free

surface distortions. The constant value of static pressure was specified at the outlet boundary.

In order to define proper boundary conditions at the inlet section, the 2D turbulent flow developing in a parallel-plate channel was computed beforehand, for each of the turbulence models examined. For those tests, the inlet free-stream turbulence intensity was set to 0.5%, and the inlet viscosity ratio was taken as 6.7. In the 2D flow computed, a position, where the boundary layer thickness δ is equal to 5.2×10^{-2} m, was found first. According to the data given in (Praisner and Smith, 2006b), this value of δ corresponded to the undisturbed (with the body removed) boundary layer at the stream-wise location of the body leading edge. Then a section located 1.5 m upstream of this position was extracted from the 2D solution and the flow field data of this section were used to define the velocity vector and turbulence parameters distributions over the inlet plane of the 3D computational domain.

In accordance with the experiments, a constant heat flux of $10,500 \text{ W/m}^2$ was specified on the endwall segment shown in Fig. 1. Remaining parts of the plate and the cylinder surface were treated as adiabatic.

3. Computational aspects

Two CFD codes of second-order accuracy were used in the present study: the commercial package ANSYS-CFX (ANSYS Inc., 2006) and the in-house code SINF (Smirnov and Zajtsev, 2004a; Smirnov and Zajtsev, 2004b). The code SINF is a well-validated block-structured Navier-Stokes solver based on the finite-volume technique using the cell-centered variable arrangement.

Several 3D non-uniform grids have been generated to study the sensitivity of numerical solutions to the grid resolution. Each grid was obtained by translation of a 2D grid along the Z-direction. The number of nodes was chosen according to the desired size of the cells nearest to the endwall, controlled by the plate-averaged value of the normalized distance, $\langle Y^+ \rangle$. The source 2D grids consisted of H- and O-structure of blocks.

In the block-structured format the grids were used for the SINF code runs. Computations with the package ANSYS-CFX were carried out on unstructured grids which hexahedral cells were identical to those of the SINF grids. Each unstructured grid was obtained as a result of the SINF grid reformatting with a specialized converter.

Table 1 provides parameters of the computational grids used. Note that the ANSYS-CFX code is based on the cell-vertex variable arrangement, in contrast to the SINF solver where the cell-centered arrangement is adopted. Consequently, for the same grid, an average Y^+ -value is half the value in the SINF code case.

Below special attention is paid to the effects of grid refinement in the planes parallel to the endwall, especially in the leading edge region where 3D vortex structures arise. In order to specify the grid quality in the LE region, a characteristic cell size, Δ^* , is introduced. In fact, Δ^* represents a typical size of the cells that are located in the vicinity of the intersection of the axis of the primary horseshoe vortex and the symmetry-plane. Note that for all the grids generated, the (X-Y)-plane cell aspect ratio in this region did not exceed 2.0. Moreover, in the vicinity of the HV axis, the cell size along the

Z-direction was adjusted to be close to Δ^* . The Δ^* -values given with respect to the body nose diameter are shown in the last column of Table 1.

4. First-stage computations: wilcox model vs. menter SST model

Initial experience of a RANS-based simulation of the flow under consideration was accumulated using the SINF code. The computations were performed with grid A1.

Fig. 2 gives a general view of the flow computed with the original Menter SST model. As clearly visible, the major peculiarities of the velocity field are attributed to the leading edge endwall region.

The symmetry-plane streamlines patterns obtained with the Wilcox and the MSST turbulence model are compared in Fig. 3. As well, isolines of the viscosity ratio computed are presented in this figure. Both the models predict the phenomenon of flow separation, with the separation point (SP) located upstream of

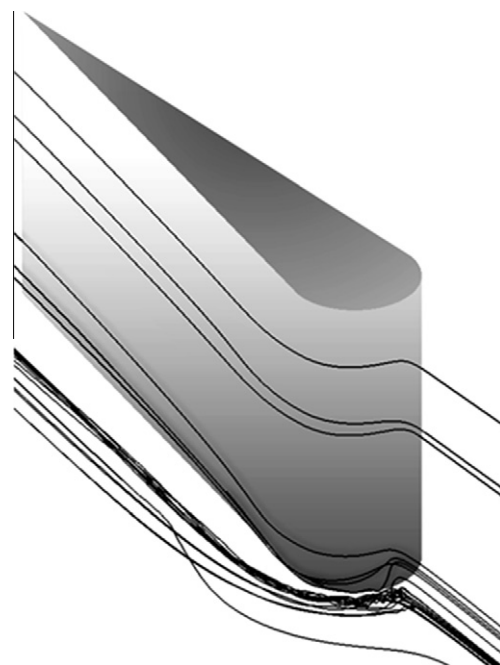


Fig. 2. Streamlines of the 3D flow around a blunt-nose body mounted on a plate.

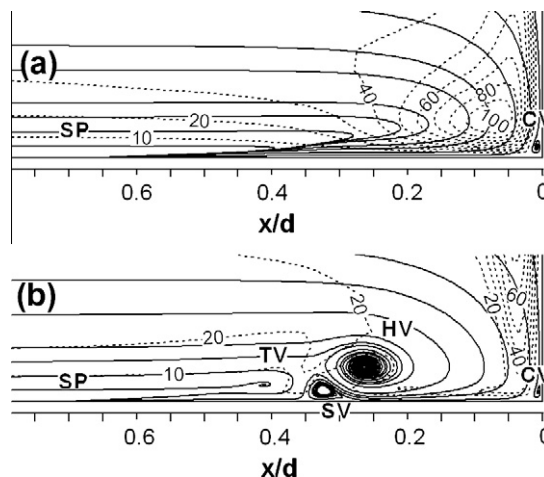


Fig. 3. Symmetry-plane streamline patterns and viscosity ratio isolines computed with (a) the Wilcox model and (b) the original version of MSST model, grid A1.

Table 1
Computational grids.

Grid	Number of cells	Nodes in Z-direction	$\langle Y^+ \rangle$ (CFX)	d/Δ^*
A1	570,000	46	1.0	100
B1	1,100,000	56	1.0	200
C1	4,100,000	79	1.0	400
A2	740,000	59	0.13	100
B2	1,400,000	68	0.13	200
C2	4,900,000	90	0.13	400

the leading edge at a distance exceeding the edge radius. One can see however that the Wilcox model predicts a rather simplified flow structure as compared with the MSST model. In the pattern obtained with the Wilcox model there are no zones with closed streamlines, except the corner vortex (CV) zone. With the same grid A1, the MSST model was able to predict development of the primary horseshoe vortex and also a counter-rotating secondary vortex located upstream.

The reason for these principal differences in the various flow patterns is the different levels of eddy-viscosity produced by the two turbulence models. In general, turbulent viscosity values given by the Wilcox model for the flow region under simulation are several times higher than in the MSST model case. An over-estimated level of the effective viscosity prevents the formation of a complex vortex structure.

The distinctions in the computed vortex structures have a pronounced effect on the local heat transfer rate. Fig. 4 presents computed variations of the endwall Stanton number, St , along the symmetry line. The St value is defined as follows:

$$St = \frac{q}{\rho V_{in} C (T_w - T_{in})} \quad (1)$$

The Wilcox model predicts a monotonic increase of St when approaching the body nose (after the separation point), whereas two St peaks are given by with MSST model, in qualitative agreement with the measurement data.

The results of the first-stage computations have led to the conclusion that the Wilcox model is not capable of predicting development of a multiple-vortex system and correct behavior of the Stanton number in the region near the blunt-nose of the body. Note that a similar conclusion was also reached after results of numerical study by Levchenya and Smirnov (2007) of 3D flow near the leading edge of turbine blades mounted on a platform. The data reported in (Levchenya and Smirnov, 2007) showed a superiority of the MSST model, but pointed also that 3D numerical solutions obtained with this model is rather sensitive to computational grid.

The MSST model was accordingly chosen for the next stage of the present study. In order to reach the more justified conclusion on the MSST model capabilities for predicting the flow under analysis, computations were also performed with the commercial package ANSYS-CFX (ANSYS Inc., 2006). Here it should be emphasized that only the modified version of the Menter SST model (Menter et al., 2003) is available in the latest releases of the ANSYS-CFX. It provided motivation to implement the modified MSST model into the SINF code as well, and to perform comparative computations of the flow with two versions of the model.

Table 2 presents computational data for several representative characteristics of the flow. This table covering also the measure-

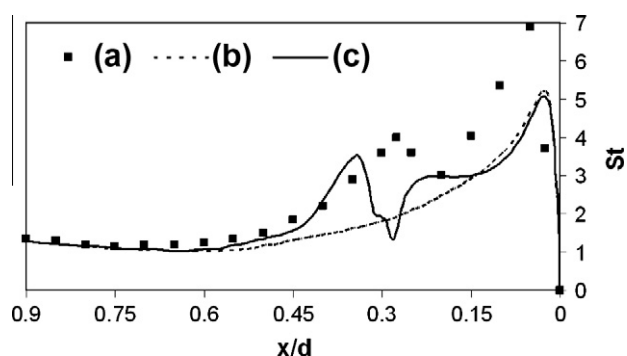


Fig. 4. Symmetry-plane endwall Stanton number distributions: (a) experiments (Praisner and Smith, 2006b), (b) Wilcox model, grid A1, and (c) original MSST model, same grid.

Table 2

Comparison of data obtained with two versions of the MSST model, grid A1.

Model	λ_s	λ_0	St_{max}
MSST (Menter, 1993)	0.694	0.263	5.0
MSST (Menter et al., 2003)	0.644	0.234	6.1
Experiments (Praisner and Smith, 2006b)	0.55	0.175	6.9

ment results gives evidence that the modified MSST model (Menter et al., 2003) has a notable superiority for prediction of this type of flows. A grid resolution study, results of which are presented in the next Section, was performed with this turbulence model version.

5. Results of refined computations using the menter SST model

5.1. Flow structure

A series of computations was carried out to investigate the question of the grid resolution effect on the separation point position. In addition to the information given in Section 3 for the grids used, note here that a typical size of the grid cells near the SP, designated hereinafter as Δ^{**} , is of about $0.035d$ for grid A1. To answer the question, one more grid, termed A1-a, was generated providing $\Delta^{**} \approx 0.013d$ while keeping all other grid quality parameters the same as in the prototype grid. The computations performed with the MSST model (Menter et al., 2003) have resulted in practically same λ_s values for grids A1 and A1-a.

For grids B1, B2, C1, and C2, the value of Δ^{**} is the same and equal to about $0.025d$ that is between the values given above for grids A1 and A1-a. As a result, one may conclude that the quality of all the grids used is sufficient to get a grid independent result for the SP position.

As noted above, one of the primary interests is the effect of grid refinement on the horseshoe vortex formation region. Fig. 5 presents symmetry-plane streamline patterns obtained (using the

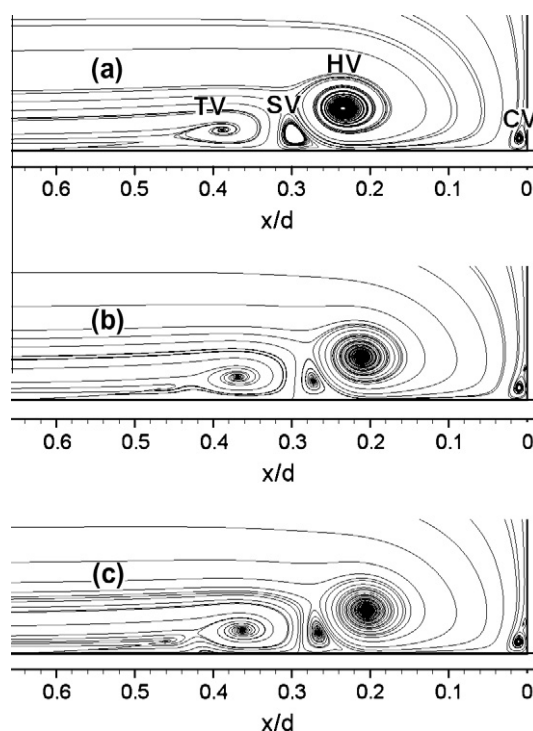


Fig. 5. Effect of grid resolution on symmetry-plane streamline pattern: (a) grid A1, (b) grid B1, and (c) grid C1.

ANSYS–CFX) with three grids characterized by considerably different values of Δ^* (see Table 1). In all the patterns given one can see multiple-vortex structures consisting of the primary horseshoe vortex, the secondary vortex, the tertiary vortex and the corner vortex. With the reduction in the Δ^* value, the tertiary vortex becomes more pronounced. In the case of the most refined grid, two additional relatively weak vortices (one clockwise and other counter clockwise) appears upstream of the tertiary vortex. Fig. 6 shows an isometric view of the multi-vortex structure computed with grid C1. To identify the vortices, the field of the Q -criterion (Hunt et al., 1988) was processed.

Fig. 7 presents a further isometric view of the flow computed. Here, in addition to the vortex-tube images, visualization of the flow is done for four planes normal to the endwall. The plane $\varphi = 90^\circ$ (left in the figure) is used to show the Q -criterion distribution, and distributions of the vorticity magnitude (s^{-1}) are shown for three other planes, $\varphi = 0^\circ, -60^\circ,$ and -90° .

Comparing the obtained steady-state RANS solutions with the experimental data from (Praisner and Smith, 2006a, 2006b), one should note that the time-averaged flow pattern given in (Praisner and Smith, 2006b) does not include a secondary vortex. However, instantaneous pictures reported in (Praisner and Smith, 2006a) show clearly the existence of secondary vortices at some instants. Under the conditions of bimodal temporal behavior of the near-

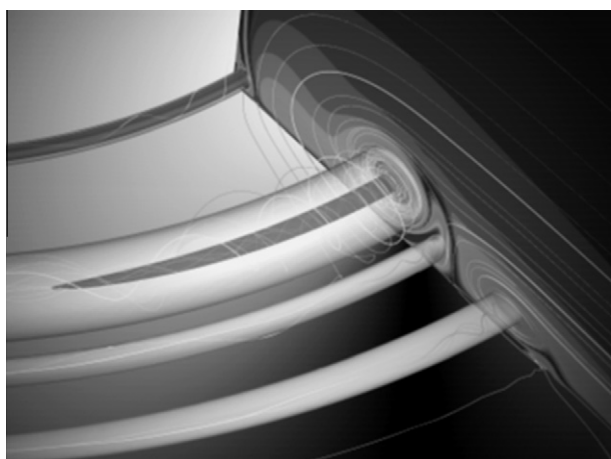


Fig. 6. Multiple-vortex structure computed for the flow region near the body leading edge. Shown streamlines are rolled around vortex cores displayed by iso-surfaces of Q -criterion: $Q = 0.5 \text{ s}^{-2}$ for light coloured vortex-tubes, and $Q = 0.9 \text{ s}^{-2}$ for dark coloured.

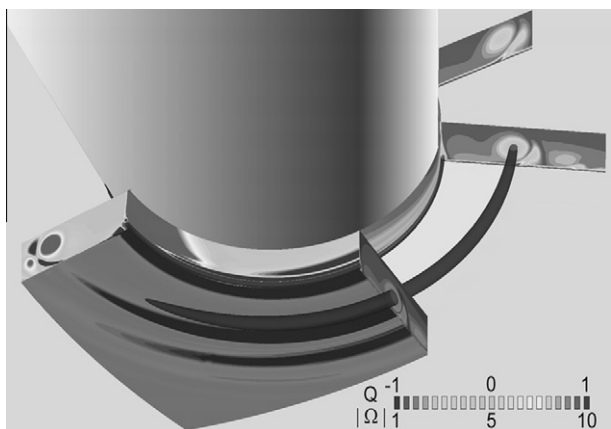


Fig. 7. Vorticity distribution in the flow region near the body leading edge.

leading-edge flow, application of the time-averaging procedure results in a considerably shaded pattern of the flow vortex structure.

Grid sensitivity of the numerical solutions is illustrated also in Fig. 8 where the data obtained with the two codes for the distance from the HV axis to the body LE are presented. Note that the experimental value of λ_0 reported in (Praisner and Smith, 2006b) is $0.175d$.

The results given in Fig. 8 for three successively refined grids (lines “a” and “b”) show that the HV axis approaches the body LE with decreasing of Δ^* . The data of lines “a” and “c” allow a direct comparison of the two CFD codes with respect to sensitivity to the Y^+ -value. Close results are obtained if for the ANSYS–CFX runs one employs grids which provide several times smaller endwall Y^+ -values compared with the SINF code case.

5.2. Endwall heat transfer

In comparison with the measurement data, Fig. 9 shows the symmetry-plane endwall Stanton number distributions computed with the two codes.

In accordance with the experiments, the computations predict two St peaks. Note that the first (lower) peak may occur in the experiments solely due to the formation of a tertiary vortex. Far away from the body, the computed St values are in a good agreement with experimental data. The global computed St peak is located closer to the LE, compared with the experiments, and generally the St values in the region adjacent to the LE are underestimated (the SINF code showed a better result).

Fig. 10 presents data for peak values of the Stanton number obtained in different computational runs (note that the experimental peak St value is about 7). There is a slight tendency for improvement of agreement with grid refinement in the XY -plane. However, the effect of this refinement is weaker than the effect of reducing Y^+ -values, especially in the case of the ANSYS–CFX code.

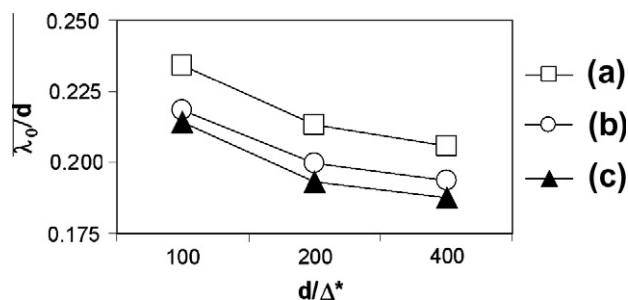


Fig. 8. Results for the distance from the HV axis to the body LE in symmetry-plane: (a) CFX, grids A1, B1, and C1; (b) CFX, grids A2, B2, and C2; and (c) SINF, grids A1, B1, and C1.

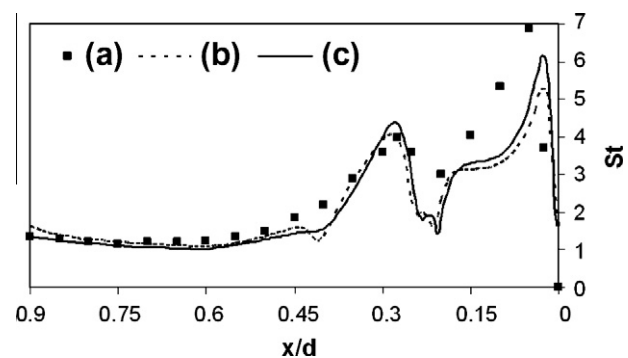


Fig. 9. Symmetry-plane endwall Stanton number distributions: (a) experiments (Praisner and Smith, 2006b); (b) CFX, grid C2; and (c) SINF, grid C1.

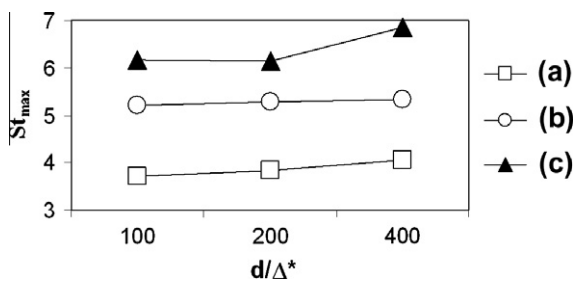


Fig. 10. Computed Stanton number peak values: (a) CFX, grids A1, B1, and C1; (b) CFX, grids A2, B2, and C2; and (c) SINF, grids A1, B1, and C1.

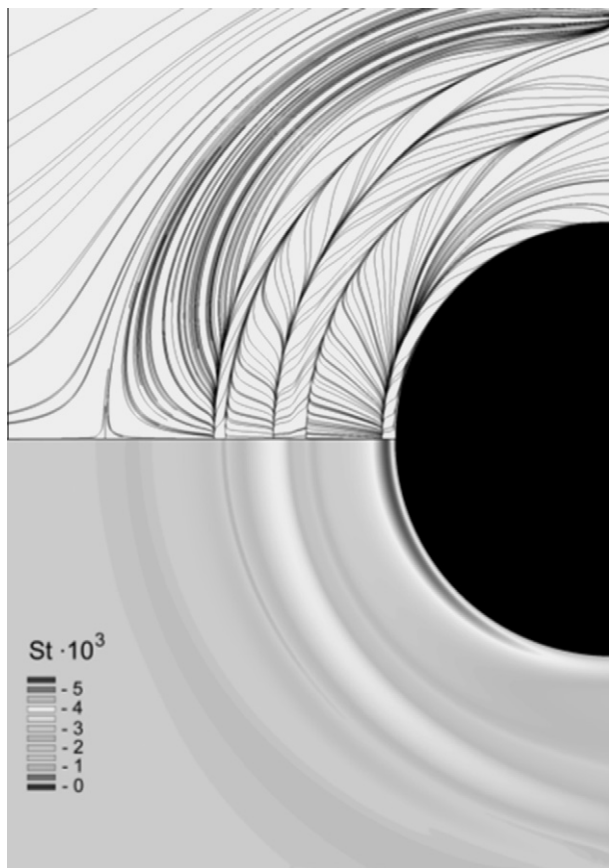


Fig. 11. Endwall streakline patterns (top) and Stanton number distribution (bottom).

Fig. 11 illustrates the endwall streaklines pattern and the end-wall St distribution simultaneously. One can see a close relationship between the individual vortex “footprints” and local peaks of the Stanton number.

6. Conclusion

Using the in-house 3D CFD code SINF and the commercial package ANSYS-CFX, systematic computations have been performed to investigate capabilities of several variants of the $k-\omega$ family turbulence models to predict peculiarities of the 3D flow field and end-wall heat transfer in the juncture of a blunt-nose body and a flat plate. The computational results were compared with the measurement data reported recently by Praisner and Smith. Special attention was paid to grid sensitivity of the numerical solutions.

It has been established that the low-Re Wilcox turbulence model is not capable of predicting the development of a multiple-vortex system observed in the experiments upstream of the body's leading edge. The simplified flow topology predicted with the Wilcox model is due to the fact that generally it overestimates the eddy-viscosity in the flow region under consideration.

Both versions of the MSST model (the original and the modified one) produce qualitatively correct results, with a considerable superiority of the modified version when comparing the quantitative data with the measurement results.

Rather fine computational grids are needed to obtain grid independent data of intensity and position of the multiple-vortex structure forming near a blunt-nose body, as well as of the endwall local heat transfer resulting from this structure. With CFD codes of second-order accuracy, to resolve the horseshoe vortex formation region, one should use grids with cells that are 2–3 order lower than the leading edge diameter.

Computational results produced by the two codes used are close to each other provided the solution convergence is achieved with respect to the Y^+ -values.

Acknowledgements

The work was partially supported by the Russian Foundation of Basic Research (Grant No. 08-08-00400), and by the Russian Federation Program for Support of Leading Scientific Schools (Grant NSH-5917.2008.8).

References

- ANSYS, 2006. CFX-Solver Theory Guide. Release 11.0. ANSYS, Inc.
- Apsley, D.D., Leschziner, M.A., 2001. Investigation of advanced turbulence models for the flow in a generic wing-body junction. *Flow, Turbulence and Combustion* 67 (1), 25–55.
- Batten, P., Craft, T.J., Leschziner, M.A., Loyau, H., 1999. Reynolds-stress-transport modeling for compressible aerodynamics applications. *AIAA Journal* 37 (7), 785–796.
- Bonnin, J.Ch., Buchal, T., Rodi, W., 1996. Data bases and testing of calculation methods for turbulent flows. *ERCOTAC Bulletin* 28, 52–53.
- Devenport, W.J., Simpson, R.L., 1990. Time-dependent and time-averaged turbulence structure near the nose of a wing-body juncture. *Journal of Fluid Mechanics* 210, 23–55.
- Hunt, J.C.R., Wray, A.A., Moin, P., 1988. Eddies, stream, and convergence zones in turbulent flows. In: *Proceeding of the Summer Program*. Center for Turbulence Research. NASA Ames/Stanford University, pp. 193–208.
- Kato, M., Launder, B.E., 1993. The modelling of turbulent flow around stationary and vibrating square cylinders. In: *Proceedings of 9th Symposium on Turbulent Shear Flows*, Kyoto, Japan, August 16–18, pp. 1041–1046.
- Levchenya, A.M., Smirnov, E.M., 2007. CFD-analysis of 3D flow structure and endwall heat transfer in a transonic turbine blade cascade: effects of grid refinement. In: *CD-ROM Proceedings of West-East High Speed Flow Field Conference – WEHSFF'07*. Moscow, Russia, 19–22 November, p. 12.
- Menter, F.R., 1993. Zonal Two-Equation $k-\omega$ Turbulence Model for Aerodynamic Flows. *AIAA Paper* 1993-2906.
- Menter, F.R., Langtry, R., Kuntz, M., 2003. Ten years of industrial experience with the SST turbulence model. *Turbulence Heat and Mass Transfer 4* (CD-ROM Proceedings).
- Praisner, T.J., Smith, C.R., 2006a. The dynamics of the horseshoe vortex and associate endwall heat transfer – Part I. Temporal behavior. *ASME Journal of Turbomachinery* 128, 747–754.
- Praisner, T.J., Smith, C.R., 2006b. The dynamics of the horseshoe vortex and associate endwall heat transfer – Part II. Time-mean results. *ASME Journal of Turbomachinery* 128, 755–762.
- Simpson, R.L., 2001. Junction flows. *Annual Review of Fluid Mechanics* 33, 415–443.
- Smirnov, E.M., Zajitsev, D.K., 2004a. The finite-volume method in application to complex-geometry fluid dynamics and heat transfer problems. *Scientific-Technical Bulletin of the St.-Petersburg State Technical University* 2 (36), 70–81 (in Russian).
- Smirnov, E., Zajitsev, D., 2004b. Computations of internal flows using an artificial-compressibility solver enhanced with an elliptic pressure-correction procedure. In: *ECCOMAS 2004*, p. 13, (CD-ROM proceedings).
- Wilcox, D.C., 1993. A two-equation turbulence model for wall-bounded and free-shear flows. *AIAA Paper* 93-2905.
- Zaitsev, D., Schur, N., Smirnov, E., Goryachev, V., 2008. Visual analysis of turbulent whirl over a cantilevered flexible blade after 3D numerical simulation. In: *13th International Symposium on Flow Visualization (ISFV13)*, Nice, France, July 1–4, p. 10, (CD-ROM Proceedings).